ACS OMEGA

Open Access

http://pubs.acs.org/journal/acsodf

Article

Rapid Fabrication of Flexible Cu@Ag Flake/SAE Composites with Exceptional EMIS and Joule Heating Performance

Zhongxin Huang, Yong Zhang,* Huipeng Wang, Yuanyuan Li, Jiewu Cui, Yan Wang, Jiaqin Liu, and Yucheng Wu*

Cite This: *ACS Omega* 2023, 8, 37032−37042

Read Online

ACCESS | Metrics & More | Article Recommendations | Supporting Information

ABSTRACT: High electromagnetic interference shielding (EMIS) effectiveness and good thermal management properties are both required to meet the rapid development of integrated electronic components. However, it remains challenging to obtain environmentally friendly and flexible films with high EMIS and thermal management performance in an efficient and scalable way. In this paper, an environmentally friendly strategy is proposed to synthesize multifunctional waterborne Cu@Ag flake conductive films using water as the solvent and silicone−acrylic emulsion (SAE) as a matrix. The obtained films show high electrical conductivity and exceptional EMI SE and electrothermal conversion properties. The EMI SE in the X-band is higher than 76.31 dB at a thickness of 60 μm owing to the ultrahigh electrical conductivity of 1073.61 S cm^{-1}. The film warms up quickly to 102.1 °C within 10 s under a low voltage of 2.0 V. In addition, the shielding coating is sufficiently flexible to retain a conductivity of 93.4% after 2000 bending−release cycles with a bending radius of 3 mm. This work presents an alternative strategy to produce high EMIS effectiveness and Joule heating films for highly integrated and flexible electronic components in a green, scalable, and highly efficient way.

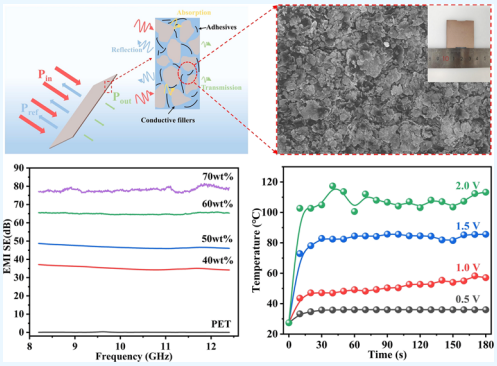

1. INTRODUCTION

With the advent of the 5G communication era, the rapid development of electronic, electrical, and communication equipment has accelerated human social processes. However, highly integrated electronic products and information equipment have caused grievous electromagnetic radiation interference, which has triggered various problems such as malfunctions or even damage to electronic devices, information security, and threats to human health.[1−3] Hence, it is of importance to develop high-performance EMI materials. Recently, increasing demands for personal thermal management, wearable heating devices, and thermal therapy have raised the research enthusiasm toward flexible, heated, and multifunctional electromagnetic shielding materials, which have great potential in both military and civilian fields.[4−7]

The composite of conductive fillers and polymers is a commonly used flexible shielding structure due to its lightweight, thin thickness, good processability, outstanding corrosion resistance, and electromagnetic interference shielding effectiveness. To achieve high EMIS properties and heat management goals, it is a crucial and challenging issue to address filler design and filler/matrix interface bonding control.[8−12]

Among various conductive fillers, carbon nanotubes,[13] MXenes,[14] copper,[15] and silver[16] powders are usually used to form conductive networks within the composites. Carbon nanotubes feature lightweight and corrosion resistance; however, they are prone to agglomeration, and their high contact resistance results in high application voltages of 4−9 V, which is unfavorable for Joule heating.[17−20] As for MXenes, it has higher electrical conductivity than CNTs, which benefits the decrease of the application voltage down to 2 V for Joule heating, but the balance temperature of most samples does not exceed 80 °C.[14,21−24] In addition, the low yield of MXenes and the complicated handling process limit their practical applications. As typical fillers for EMIS, copper and silver particles have been comprehensively investigated owing to their excellent electrical and thermal conductivity as well as desirable reliability.[25,26] For example, Choi[15] produced a layer-by-layer assembly of copper nanosheets, and the obtained Cu film exhibited an electromagnetic shielding effectiveness of 100 dB at a thickness of 15 μm. Liu[27] loaded Cu@Ag nanosheets onto a leather substrate by the spraying method, and the leather showed an EMI SE of 90 dB in the X-band at a loading of 5.17 v%. Nevertheless, copper fillers suffer from suscepti-

Received: June 21, 2023
Accepted: September 14, 2023
Published: September 26, 2023

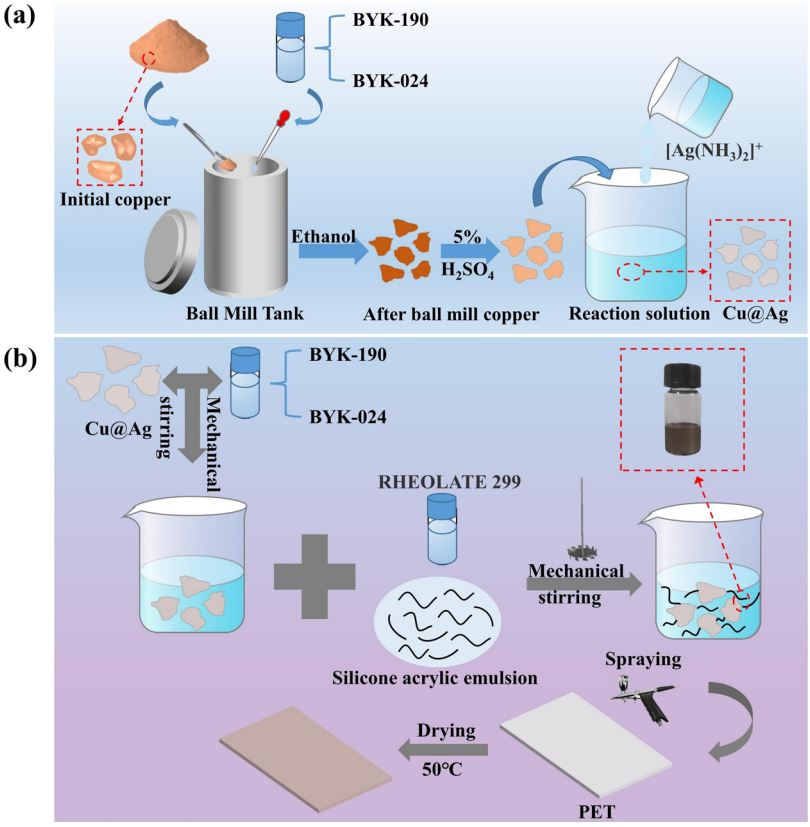

Figure 1. (a) Schematic diagram of the synthesis of Cu@Ag flakes with a core−shell structure. (b) Schematic of the fabrication for Cu@Ag/waterborne silicone−acrylic emulsion films.

bility to corrosion, while silver has additional weight as well as high cost. Therefore, architecture design is an essential issue when copper and silver are employed. Besides, a facile and highly efficient manufacturing process is necessary as well.

In terms of a matrix for hosting conductive fillers, organic media are usually utilized for metal ink production to obtain the required wettability and dispersibility of metal fillers;[28−30] however, volatile organic compounds (VOCs) are generated and released into the atmosphere,[31] which may cause serious environment concerns. Therefore, it is of great interest to develop environmentally friendly aqueous shielding coatings.[32]

In this work, an environmentally friendly water-based conductive composite was obtained with high electromagnetic shielding effectiveness, superior Joule heating capacity, and exceptional flexibility. The Cu@Ag core−shell flake filler was produced by a fast ball milling process, followed by electroless plating. The obtained core−shell flake fillers feature the following advantages: (1) The Cu core/Ag shell nanoarchitecture can combine the virtues of the two components with regard to corrosion resistance and cost-effectiveness as well as a large phase interface, which may benefit the EMI SE. (2) The two-dimensional shape of the fillers favors the assembly of the flakes to construct porous multilayered 2D architecture. The stacking core−shell layers may increase multiple internal reflection paths of electromagnetic wave, achieving a reliably high shielding performance. (3) Considering the low conductivity of the polymer matrix, the metallic flake fillers are conducive to constructing a 3D conductive network, thereby ensuring a high Joule heating effect. A waterborne silicone−acrylic emulsion was chosen as the binder, which has remarkable advantages of waterproof, anticorrosion, and aging resistance as well as cos-effectiveness.[33,34]

The results showed that the Cu@Ag core−shell structure contained only 13.7 wt % Ag and exhibited excellent corrosion resistance. The Cu@Ag flake/SAE composite film exhibited an excellent conductivity of 1073.61 S cm^{-1} at a thickness of 60 μm. The X-band EMI SE was higher than 76.31 dB and reached 81.54 dB at 11.85 GHz. Furthermore, the surface of the film can warm up to 102.1 °C in 10 s by applying a voltage of 2 V. The film maintained a conductivity of 93.40% after 2000 bending−release cycles, showing good flexibility.

2. EXPERIMENTAL SECTION

2.1. Materials. Commercial copper powder (R008036, 200 mesh) and potassium sodium tartrate were supplied by Shanghai Yi'en Chemical Technology Co. Silver nitrate and ammonia (28 wt %) were obtained from Sinopharm Chemical Reagent Co. A waterborne silicone−acrylic emulsion (NM416, 48% solid content) was purchased from Qingdao Dayang Haiderun Building Materials Co. The dispersant (BYK-190, 40% solid content), antifoamer (BYK-024, 95% solid content), and thickener (RHEOLATE 299, 25% solid content) were from Shenzhen Jin Tenglong Industrial Co. No further purification of the reagents mentioned above was required.

2.2. Synthesis of Cu@Ag Flake. The commercial copper powder (3 g), dispersant (0.54 g), antifoamer (0.012 g), and deionized water (1.5 mL) were mixed and ball-milled for 20 min. Ethanol was used to wash the ball-milled copper powder six times. Subsequently, the copper powder was comixed with 30 mL of 5% sulfuric acid solution and stirred magnetically for 1 h, washed by centrifugation using deionized water to a pH of

https://doi.org/10.1021/acsomega.3c04404
ACS Omega 2023, 8, 37032−37042

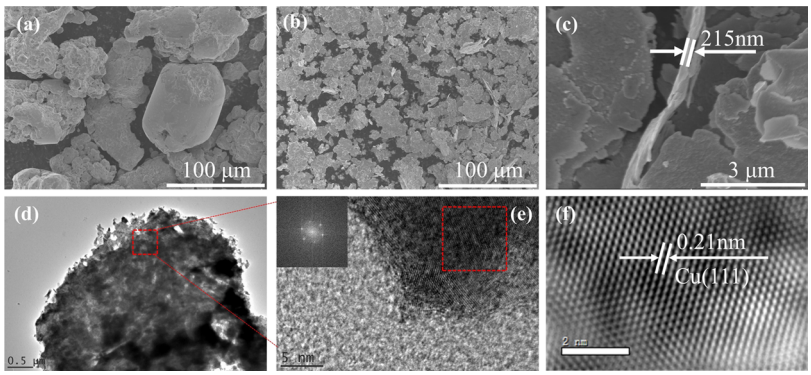

Figure 2. (a) SEM image of the original copper powder. (b) SEM image of 200 mesh copper powder after ball milling. (c) Thickness of the copper flake. (d) TEM image of the copper flake. (e) HRTEM of the copper flake. and (f) HRTEM of the sample after Fourier transform.

7.0, and dried at 60 °C for 6 h in a vacuum drying oven. After ball milling, copper powder (10 g) was added to deionized water (150 mL) to form a dispersion. Potassium sodium tartrate solution (20 mL, 1.42 mol/L) was added at a constant temperature of 30 °C and stirred at 400 rpm for 5 min; silver ammonia solution (60 mL, 0.25 mol/L) was added drop by drop. The pH of the solution was adjusted to 9−10 with ammonia, and the reaction was stirred for 30 min. The solid product was washed by centrifugation with deionized water and ethanol three times and dried in a vacuum oven at 60 °C for 10 h. Commercial copper powder without ball milling was covered with silver using the same electroless plating method.

2.3. Preparation of Cu@Ag/Waterborne Silicone−Acrylic Emulsion Films. First, Cu@Ag (0.498, 0.747, 1.121, 1.744 g), dispersant (0.35 g), antifoamer (0.012 g), and deionized water (1.5 mL) were stirred mechanically at 750 rpm for 10 min. Then, after adding the waterborne silicone−acrylic emulsion and thickener, the mixture was stirred continuously for 20 min to obtain the Cu@Ag/waterborne silicone−acrylic emulsion (SAE) conductive composite (as shown in the inset in Figure 1b). Finally, the prepared paint was transferred to a spray gun (10 cm from the substrate). The coating was slowly and uniformly sprayed onto the PET substrate (3.5 cm × 3.5 cm) and the PI flexible substrate (5 cm × 1.5 cm) to form a film. The substrates were transferred into a blast drying oven and dried at 50 °C for 30 min to acquire conductive films. After ball milling, the commercial copper powder was converted from granules to flakes (shown in Figure 2a,b). Therefore, the composite films were described as G-*x*Cu@Ag/SAE or F-*x*Cu@Ag/SAE, where *x* stands for the solid content of Cu@Ag in the films. For instance, 0.498, 0.747, 1.121, and 1.744 g of the filler correspond to 40, 50, 60, and 70, respectively.

2.4. Characterization. The crystal structures of the Cu powder and Cu@Ag flake were characterized by an X-ray diffraction analyzer (PANalytical X-Pert PRO MPD, the Netherlands) equipped with a diffractometer with a Cu Kα radiation source (λ = 1.54 Å). The particle size distribution of the ball milling copper powder was characterized by a laser particle size meter (Mastersizer 2000, Malvern Instruments, UK). Scanning electron microscopy (Hitachi SU8020, Japan) was used to observe the morphology of Cu and Cu@Ag as well as the morphology of the conductive composite films. The HRTEM image was obtained by field emission transmission electron microscopy (JEM-2100F, Japan). The conductivity of the Cu@Ag/SAE films was measured at room temperature by a four-point probe instrument (FT-340, Ningbo Ruike Weiye Instruments Co., Ltd., China). Six different locations were selected for each sample for measurement to determine the average conductivity.

The EMI SE of Cu@Ag/SAE films in the X-band (8.2−12.4 GHz) was measured using a vector network analyzer (ZNA 43, Rohde & Schwarz, Germany) in conjunction with a waveguide holder (WR-90, XinChen Technology Co., Ltd., China). Samples sprayed on PET substrates were clamped directly in the middle of the waveguide holder while bolting the fixture to ensure test accuracy. The *S* scattering parameters measured by the vector network analyzer were recorded, and power coefficients for reflection (R), transmission (T), and absorption (A) were calculated,[35] where the scattering coefficients are given by S_{11} (input reflection), S_{12} (reverse transmission), S_{21} (forward transmission), and S_{22} (output reflection). The total EMI shielding effectiveness (SE_T), the absorption shielding effectiveness (SE_A), and the reflection shielding effectiveness (SE_R) are determined according to the following equations.[36]

$$R = |S_{11}|^2 = |S_{22}|^2 \quad (1)$$

$$T = |S_{21}|^2 = |S_{12}|^2 \quad (2)$$

$$A + R + T = 1 \quad (3)$$

$$SE_R = 10 \log (1 - R) \quad (4)$$

$$SE_A = -10 \log \left(\frac{T}{1 - R} \right) \quad (5)$$

$$SE_T = SE_R + SE_A \quad (6)$$

A DC-regulated power supply (GPC-6030D, GWINSTEK, China) was used to apply voltage to both ends of the films. The Joule heating properties of the Cu@Ag/SAE films were recorded by using an infrared thermal camera (Ti480PRO, FLUKE).

3. RESULTS AND DISCUSSION

3.1. Cu@Ag Flake with a Core−Shell Structure. As shown in SEM Figure 2a,b, only after 20 min of ball milling treatment was the original copper powder transformed from large-size particles to small-size flakes with an average thickness of around 215 nm (Figure 2c), and the average size of flakes was reduced from 73 to 15 μm (Figure S1). Figure 2d shows a TEM image of the copper flake, and the red rectangular region was selected for high-resolution lattice stripe imaging, as shown

https://doi.org/10.1021/acsomega.3c04404
ACS Omega 2023, 8, 37032−37042

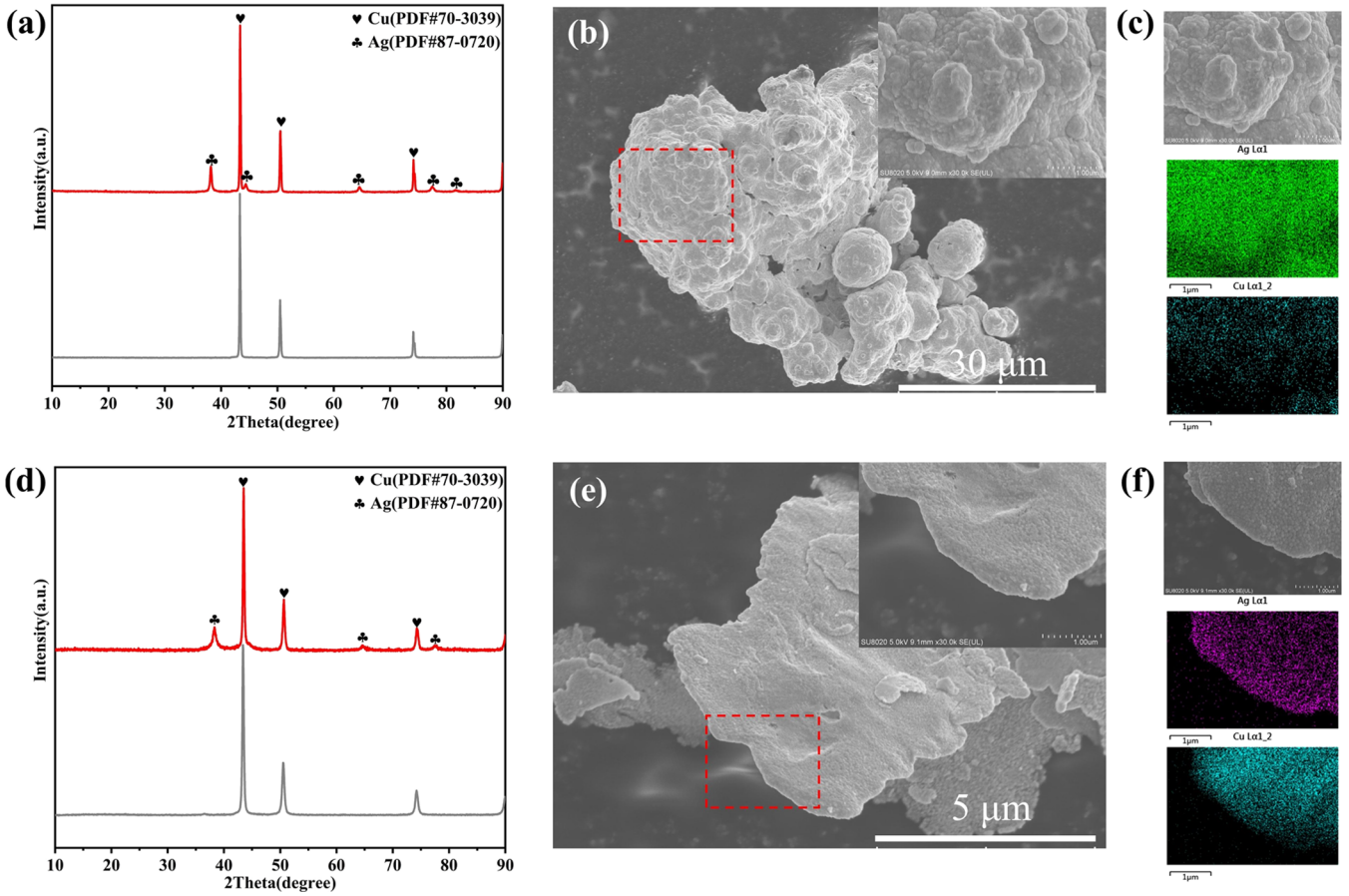

Figure 3. (a) XRD patterns of Cu and Cu@Ag at 200 mesh. (b,c) SEM and EDS images of Cu@Ag at 200 mesh. (d) XRD patterns of Cu and the Cu@Ag flake. (e,f) SEM and EDS images of the Cu@Ag core−shell flake.

in Figure 2e. Fourier transform was performed on the rectangular region of Figure 2e, and the results are shown in Figure 2f, showing a lattice distance of 0.21 nm, which corresponds to the (111) crystal plane of copper. During ball milling, the copper powder is blended, cold-welded, and fragmented repeatedly. Since copper is a ductile metal, the copper powder is supposed to get coarser due to cold welding on milling. Therefore, the ball milling was conducted under an air atmosphere to obtain copper flakes. On the one hand, the thin oxide layer generated on the copper surface made the powder brittle and allowed the formation of surface defects by limiting the welding process, which favored the formation of plate-like powder (Figure S2);[37,38] on the other hand, it is noteworthy that the ball milling time was greatly reduced benefiting from the milling additives, which can efficiently absorb on the exposed plane and hinder the plate-like powder aggregation, thereby speeding up the grinding efficiency. Meanwhile, the ball milling treatment improved the hydrophilicity of the copper powder, and Figure S3a,b demonstrates that the water contact angle of the original copper powder was reduced from 86.7 to 80.7°. This is due to the large amount of surface energy, interfacial energy, and distortion energy accumulated in the powder as a result of the milling procedure. The high surface energy of a solid makes it easier for a lower-energy liquid to spread out on top of it, which in turn decreases the energy of the system.[39,40] Infrared spectroscopy of the washed copper flake shows no characteristic absorption peaks of the chemical groups, as observed in Figure S3c, further indicating that the additives were introduced to improve the ball milling efficiency. In addition, wet ball milling not only refines the copper powder particles but also reduces the loose density of the powder from 2.381 to 0.735 g/cm^3 (Figure S4a). It is visualized in Figure S4b that the ball-milled copper powder occupies a larger volume than the original copper powder when 5 ± 0.0005 g of copper powder is weighed.

The Cu@Ag core−shell structure was synthesized by using electroless plating. Silver ammonia solutions were prepared using silver nitrate as the silver source and $NH_3{\cdot}H_2O$ as the complexing agent. The reducing agent, sodium potassium tartrate, reduces $Ag[(NH_3)_2]^+$ to Ag particles deposited on the Cu surface to form Cu@Ag core−shell flakes.

Figure 3a,d displays the X-ray diffraction analysis of granular Cu and Cu@Ag and Cu and Cu@Ag flake, respectively. The diffraction peaks at 43.341, 50.478, and 74.172° correspond to the (111), (200), and (220) diffraction planes of face-centered cubic Cu (PDF#70−3039), respectively. Figure 3a exhibits diffraction peaks at 38.200, 44.400, 64.600, 77.597, and 81.755° corresponding to the (111), (200), (220), (311), and (222) crystal planes of face center cubic Ag (PDF#87−0270), respectively. The diffraction peaks appearing at 38.200, 64.600, and 77.597° are shown in Figure 3d. The Cu flake had a larger surface area than the granular Cu powder, and therefore, the Cu flake was coated by a less thin silver layer than Cu powder. Figure 3b,e shows the morphology of the Cu@Ag granule and flake, respectively. The Ag particles could not be directly identified due to the rough surface of the granular copper. Figure 3c directly shows the Cu powder

https://doi.org/10.1021/acsomega.3c04404
ACS Omega 2023, 8, 37032−37042

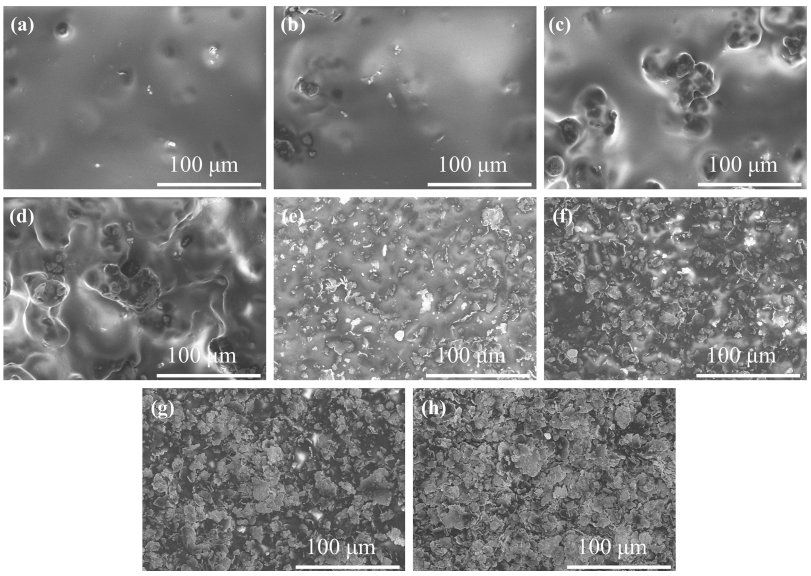

Figure 4. 500× SEM images of (a)−(d) G-40Cu@Ag, G-50Cu@Ag, G-60Cu@Ag, and G-70Cu@Ag and (e)−(h) F-40Cu@Ag, F-50Cu@Ag, F-60Cu@Ag, and F-70Cu@Ag, respectively.

surface covered with a silver layer, which proves the formation of a Cu@Ag core−shell structure. Figure 3b shows the morphology of granular Cu@Ag. However, the silver particles could not be directly identified because of the rough surface of granular Cu. Combined with the EDS analysis, Figure 3c directly displays the surface of copper powder covered with a silver layer, which proves the formation of the Cu@Ag core−shell structure. The surface of the copper flake was smooth (Figure S6), and the Cu@Ag core−shell structure can be directly observed in Figure 3e. Figure 3f indicates that Ag is uniformly distributed on the surface of the Cu flake, and a uniform silver layer is obtained. The Cu@Ag configuration contained only 13.97 wt % silver, significantly reducing the amount of silver used, as shown in Figure S7. To compare the stability of the copper−silver core−shell structure and copper flake fillers, newly synthesized copper−silver core−shell flakes and copper flakes were both put into an air drying oven instead of a vacuum oven at 50 °C for 30 min, mimicking the drying conditions of the EMI coating. After the treatment, the surface of the copper flakes became dark due to corrosion, while the color of the Cu@Ag flakes remained unchanged. To evaluate the corrosion resistance of the Cu@Ag flakes, the surface chemical state of the flakes was further analyzed using XPS. The XPS analysis in Figure S8a,d reveals characteristic peaks at 374.50 and 368.49 eV, which correspond to Ag $3d_{3/2}$ and Ag $3d_{5/2}$, respectively, confirming the presence of metallic (zerovalent) silver. Figure S8b,e presents the XPS spectra of copper elements in the sample before and after aging, respectively. The characteristic peaks at 934.59 and 953.70 eV correspond to $Cu^{2+}2p_{3/2}$ and $Cu^{2+}2p_{1/2}$, respectively. Auger peak analysis in Figure S8c,f shows that the Auger peaks at 913.11 and 917.61 eV correspond to Cu^0 and Cu^+, respectively. This indicates the coexistence of metallic copper and monovalent copper.[41] Therefore, the two peaks at 952.49 and 932.73 eV correspond to Cu^0 $2p_{3/2}$/Cu^+ $2p_{3/2}$ and Cu^0 $2p_{1/2}$/Cu^+ $2p_{1/2}$, respectively. It is worth noting that the peak area of Cu^{2+} slightly increases after aging, while the peak intensity of Cu^0 remains significantly larger than that of Cu^+. This indicates that only a small portion of the Cu@Ag structure oxidizes after aging, thereby demonstrating the good corrosion resistance of the Cu@Ag core−shell sheet.

3.2. Morphology of Cu@Ag/SAE Films. Waterborne conductive paints were prepared by mixing Cu@Ag, dispersants, antifoamers, thickeners, and silicone−acrylic emulsions. The dispersant could reduce the surface tension of Cu@Ag, the thickener adjusted the viscosity of the system and prevented the conductive filler from settling and aggregating during drying, and the silicone−propylene emulsion was used as a polymer binder to provide fastness and softness to the conductive film. Cu@Ag/SAE films with adjustable conductivity were obtained by spraying the coating on PET substrates. Figure 4 shows the microscopic morphology of the films with different Cu@Ag contents. The surface morphology of the resulting Cu@Ag/SAE coating displays that the granular Cu@Ag was sparsely dispersed in the film due to its high bulk density, and the interconnection effect between the particles was poor, making it difficult to form an effective conductive network. With the increase of conductive fillers, more and more Cu@Ag flakes were dispersed on the surface of the coating, the number of contacts between them increased, and the spacing decreased. Concurrently, the density of the film surface also gradually increased, and the conductive network formed by the close arrangement between the fillers became increasingly complete. Especially when the Cu@Ag content enlarged to 70 wt % (Figure 4h), the F-70Cu@Ag/SAE coating surface was almost completely covered by Cu@Ag flakes, which would construct more electron transfer paths.

3.3. EMI Shielding Performance of Cu@Ag/SAE Films. Figure 5a exhibits the conductivity of the Cu@Ag/SAE composite films. Clearly, the conductivity gradually enhanced with the increase of Cu@Ag content. For the G-Cu@Ag/SAE films, no conductive pathways were developed for the 40−60 wt % filler (as shown in Figure 4a−c), so the values could not be detected. 70 wt % of the filler formed a sparse conductive network with a conductivity of 79.66 S cm^{-1}. Interestingly, for the F-40Cu@Ag/SAE film, the conductivity reached 77.39 S cm^{-1} despite the low filler content. Interestingly, for the F-40Cu@Ag/SAE film, the conductivity reached 77.39 S cm^{-1} despite the low filler content due to the fact that Cu@Ag flakes

https://doi.org/10.1021/acsomega.3c04404
ACS Omega 2023, 8, 37032−37042

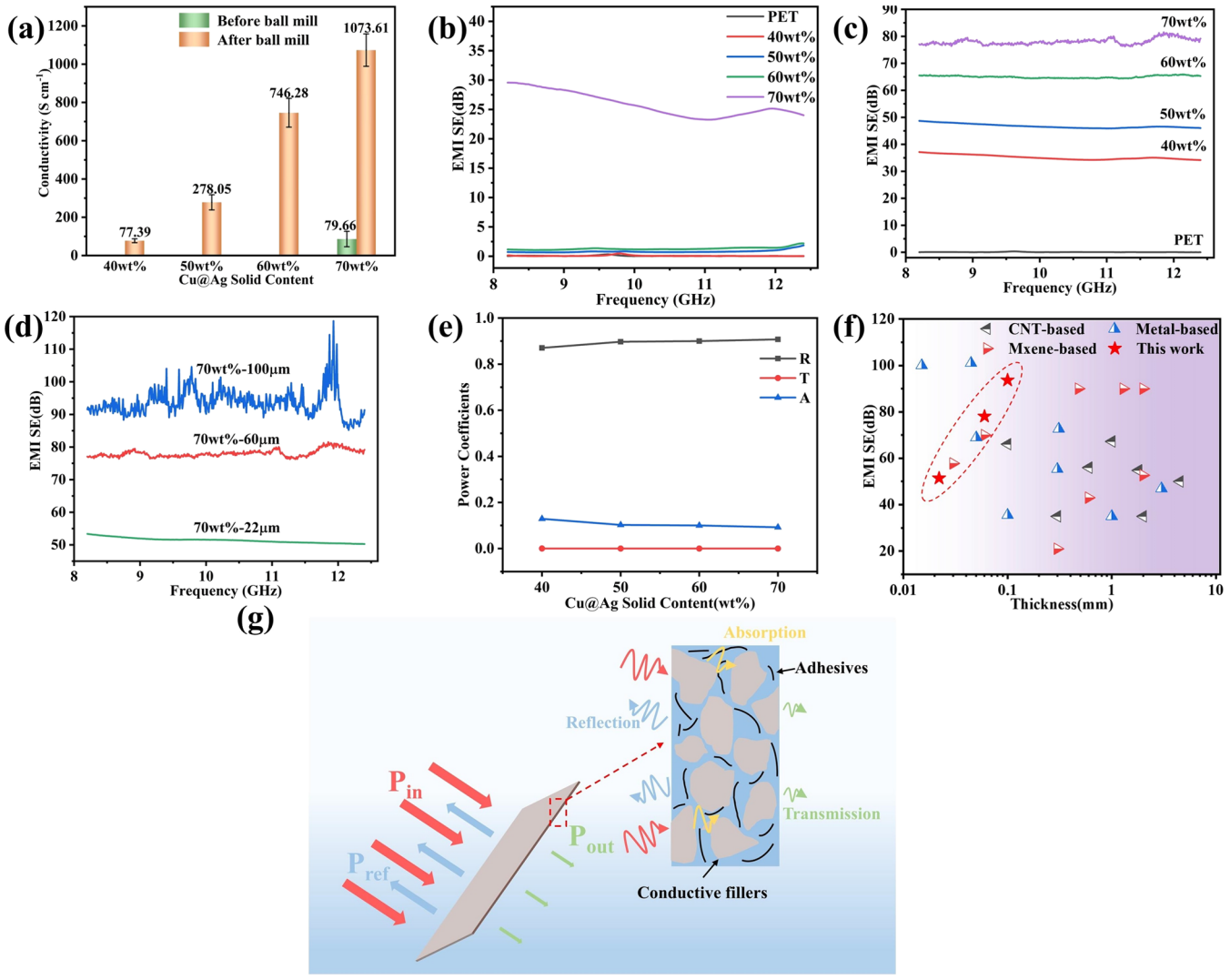

Figure 5. (a) Electrical conductivity of Cu@Ag/SAE films. (b) EMI SE of G-Cu@Ag/SAE films and PET. (c) EMI SE of F−Cu@Ag/SAE films and PET. (d) EMI SE of F-70Cu@Ag/SAE films with different thicknesses. (e) R, A, and T coefficients. (f) Comparison of the EMI SE of the other shielding materials in previous reports with our work. (g) Schematic diagram of the EM shielding of Cu@Ag/SAE films.

possess higher interconnectivity compared to granular structures. As the filler content increased to 50 and 60 wt %, the conductivity further reached 278.05 and 746.28 S cm^{-1}, respectively. Notably, the conductivity of the film with 50 wt % Cu@Ag core−shell flakes was 200.66 S/cm higher than the case when 40 wt % Cu@Ag core−shell flakes were used. This indicates that the percolation threshold was reached in the film containing 50 wt % Cu@Ag core−shell flakes. When it enlarged to 70 wt %, the ultrahigh conductivity was 1073.61 S cm^{-1}. A complete and effective conductive network gives an excellent EMI SE of Cu@Ag/SAE films.

Figure 5b shows the shielding ability of the G-Cu@Ag/SAE coating on the PET substrate and the original PET substrate against electromagnetic waves. Obviously, PET is a wave-transparent material that has almost no shielding capability. There was merely 23.25 dB (11.05 GHz) EMI SE for the G-70Cu@Ag/SAE film. There was merely 23.25 dB (11.05 GHz) EMI SE for the G-70Cu@Ag/SAE film, due to the complete and efficient electronic transmission path was not established. Figure 5c displays that the F−Cu@Ag/SAE coating has an excellent EMI SE, which increases significantly with increasing filler content. For example, in the X-band, the F-40Cu@Ag/SAE coating possessed above 34.18 dB (12.40 GHz) EMI SE, which far exceeded the standard value of 20 dB for commercial applications.[42] The EMI SE further exceeded 45.9 dB (11.02 GHz) and 64.35 dB (11.18 GHz) when the filler content increased to 50 and 60 wt %, respectively. The F-70Cu@Ag/SAE film of 60 μm (Figure S9) obtained an excellent 76.31 dB (11.38 GHz) EMI SE, which is sufficient to block 99.9999976% of the incident electromagnetic wave.[43]

For F−Cu@Ag/SAE films with consistent filler solid content, the EMI SE is positively correlated with the coating thickness,[35] which can be visualized in Figure 5d. When the thickness of the F-70Cu@Ag/SAE coating increased from 22 to 100 μm, the average EMI SE boosted significantly from 51.41 to 93.66 dB, respectively. It can be seen that the EMI SE of the sample exceeded 90−100 dB. In this case, the signal was quite sensitive to background noise, almost approaching the test limit of the instrument at the test parameter settings (Table S1). Hence, the EMI SE plot was not smooth in this situation. The EMI SE was enhanced because the increase in thickness brought more layers of filler arrangement, which improved the ability to reflect electromagnetic waves. In addition, the EMI SE of Ag powder (200 mesh) and Cu flakes

https://doi.org/10.1021/acsomega.3c04404
ACS Omega 2023, 8, 37032−37042

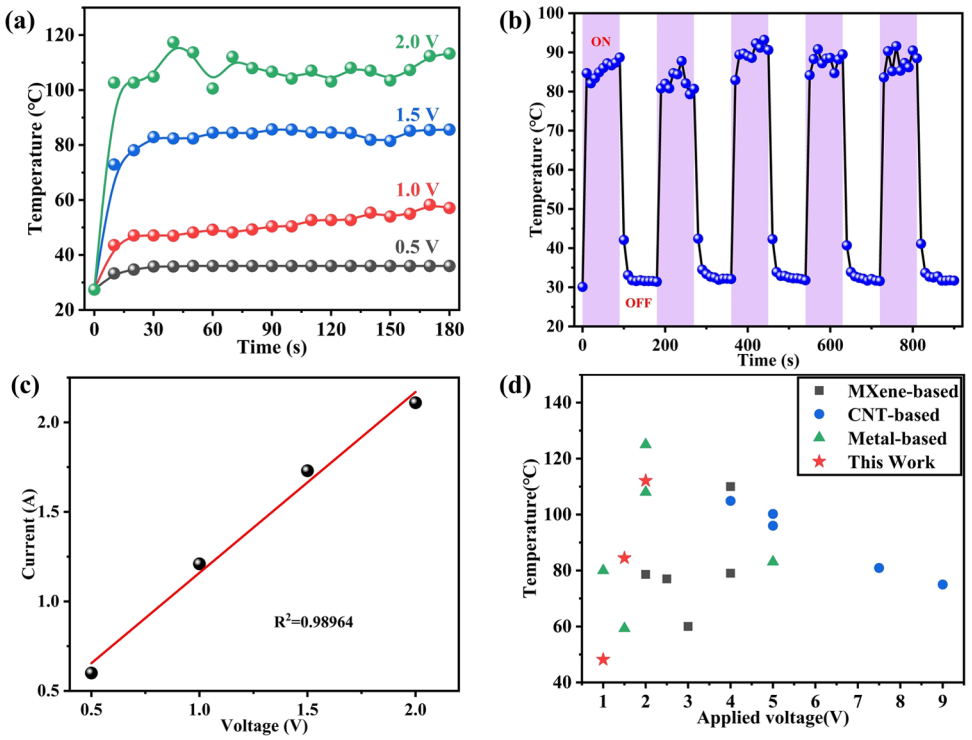

Figure 6. (a) Temperature variation of Cu@Ag/SAE films at 0.5−2 V applied voltages. (b) Cyclic heating−cooling process of the film at 1.5 V. (c) Voltage−current curve. (d) Comparison of Joule heating performance of the other materials with this work.

at a 70% filling amount (Figure S10a) was compared. Since the silver powder was completely dispersed inside the film (Figure S10b), the film shows a nonconducting state, and the EMI shielding effectiveness of the Ag/SAE film was close to 0. Interestingly, despite the addition of 70 wt % granular Ag, the composites still did not reach the percolation threshold. The advantages of the flaky core−shell structure as a conductive filler were further confirmed. The EMI shielding effectiveness of the Cu/SAE film was 3.85 dB (11.12 GHz) despite the formation of an effective lap between the copper flake (Figure S10c). This is due to the poor oxidation resistance of the copper flake, where copper has been converted to non-conductive copper oxide. Figure 5g illustrates the shielding schematic diagram of the Cu@Ag/SAE coating. Due to the effective connection of Cu@Ag, a continuous and efficient conductive network was formed inside the composite film. When electromagnetic waves are incident on the surface of the film, an impedance mismatch occurs between the coating and free space, and the vast majority of the electromagnetic waves are reflected back.[44] The remaining electromagnetic waves enter the interior of the material and interact with Cu@Ag/SAE. The heterogeneous structure within the coating provides a large interfacial region for repeated reflection and scattering of electromagnetic waves, which prolongs the electromagnetic wave transmission path and generates an effective absorption loss. Eventually, slight electromagnetic waves penetrate the coating. To further explain the shielding mechanism of the samples, the reflection (R), absorption (A), and transmission (T) coefficients were introduced.[36] Figure 5e demonstrates the values of A, R, and T for F−Cu@Ag/SAE films. The coefficients are calculated from the measured scattering parameters and eqs 1−3. As the conductive filler increased, the reflection coefficient R increased and the absorption coefficient A decreased, and R (>0.87) was much larger than A. This further indicated that the coating undergoes an impedance mismatch with the free space, and more than 87% of the electromagnetic waves were reflected back. Therefore, it can be shown that reflection plays a dominant role in EMI shielding performance. It should be mentioned that the F-70Cu@Ag/SAE film showed an electromagnetic wave reflectance of around 0.87 at an EMI SE of 76.31 dB in spite of its high conductivity, which is much lower than the reflectivity value of dense and highly conductive layers with similar EMI SE. This indicates that stacking layers of the core−shell flakes were arranged in the EMI film in which a cavity structure was formed and absorption of electromagnetic waves was enhanced. To evaluate the level of EMI SE excellence of Cu@Ag/SAE thin films, CNT-based, MXene-based, and metal-based electromagnetic shielding materials reported by others were compared (Table S2). As shown in the EMI SE comparison in Figure 5f, the EMI SE of Cu@Ag/SAE films outperformed most of the reported materials at similar thicknesses. This was mainly attributed to the effective connection of the Cu@Ag flake in the film, which provided excellent conductivity and outstanding EMI SE. Therefore, this work provides an important idea for the next generation of efficient electromagnetic shielding materials.

3.4. Electrothermal Performance of F−Cu@Ag/SAE Films. The ultrahigh conductivity Cu@Ag/SAE films not only achieve outstanding EMI shielding effectiveness but also possess excellent Joule heating properties. Figure 6a presents the Joule heating performance of the F-70Cu@Ag/SAE film (40 mm × 15 mm × 0.06 mm) when different voltages were applied, and the temperature was recorded once at 10 s intervals by using an infrared thermal camera. Since the 0.5 V voltage was excessively low, the saturation temperature of the electrothermal conversion was kept at 36 °C. With the gradual improvement of the driving voltage, the saturation temperature

https://doi.org/10.1021/acsomega.3c04404
ACS Omega 2023, 8, 37032−37042

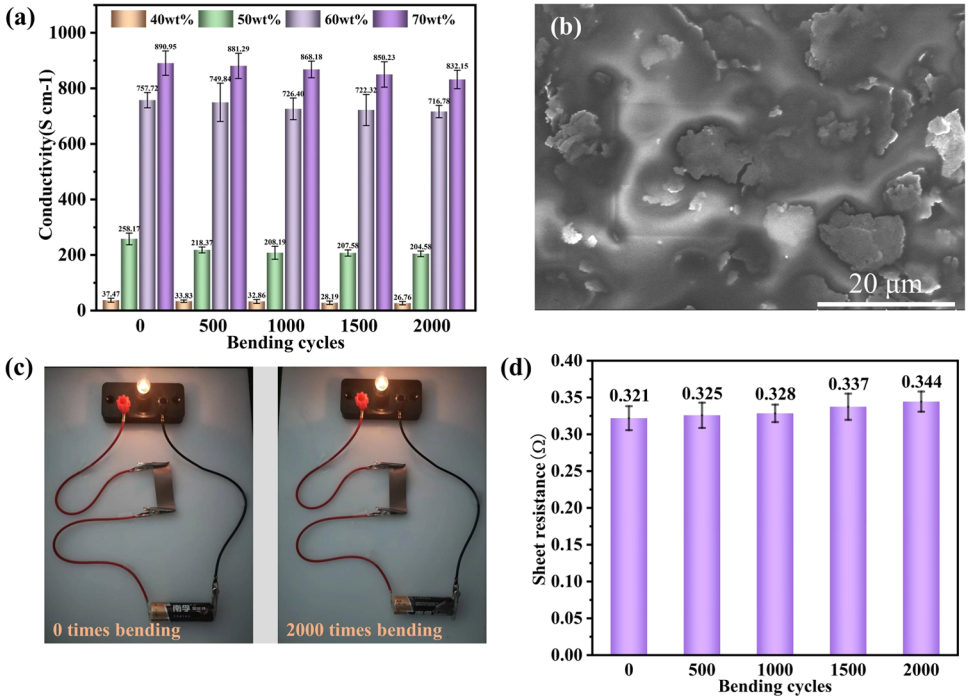

Figure 7. (a) Variation of conductivity of the film for different numbers of bending−release cycles. (b) SEM image of the F-50Cu@Ag/SAE film after 2000 bending−release cycles. (c) Changes of bulb brightness for 0 and 2000 bending−release cycles of the film. (d) Variation of square resistance for different numbers of bending−release cycles.

gradually increased to 48.2 °C (1 V), 84.5 °C (1.5 V), and finally to 112.1 °C (2 V). Hence, the Cu@Ag/SAE film had a highly efficient electrothermal conversion efficiency. In addition, the cyclic application of 1.5 V to the conductive film, as shown in Figure 6b, exhibited almost no change in its performance, indicating good cyclic stability of the Joule heating performance. As illustrated in Figure 6c, the voltage versus current is linear, in high agreement with Ohm's law, indicating that the film has a modulated and controllable Joule heating performance. For a more visual observation of the electrothermal conversion performance, Figure S11a illustrates the melting process of a wax ring (7 mm outer diameter, 3.04 mm inner diameter, 1.5 mm thickness, and 62−64 °C melting point) under 1.5 V. Due to the fast response rate, a trace melting of the wax started at the bottom at 30 s of operation, and after 60 s, a significant melting of the wax occurred owing to the accumulation of heat. As time continued, the wax was further melted, and finally, at 223 s of operation, the paraffin wax was completely melted. There is excellent water resistance for the silicone−acrylic emulsion. Consequently, Cu@Ag/SAE films can also be extended to the deicing environment, which indicates a certain practical application in the electrothermal field. Meanwhile, we also tested the electrothermal conversion performance of the films with other filler ratios, as shown in Figure S12. The electrothermal conversion efficiency of F-40Cu@Ag/SAE and F-50Cu@Ag/SAE is low because the filler ratio is not high, and the films do not have a perfect conductive pathway. As shown in Figure S12b, the heating temperature of the F-50Cu@Ag/SAE film is lower than 36 °C at a voltage of 2 V. With the increase of filler, the resistance of the sample further decreased, and the F-60Cu@Ag/SAE film demonstrated good Joule thermal performance. At 2 V, the sample showed a good response speed with a rapid temperature increase to 93 °C within 10 s. In addition, Figure S12d−f demonstrates a linear relationship between voltage and current, again indicating that the films have a controllable Joule heating performance. Compared with other previously reported Joule heating materials (e.g., Figure 6d), such as MXene-, CNT-, and Ag-based composites (Table S3), our Joule heating performance is further highlighted.

3.5. Flexibility Performance of F−Cu@Ag/SAE Films.

For the purpose of exploring the potential application of Cu@Ag/SAE films in the field of flexible wearables, the flexibility performance of the samples was characterized in this work. The Cu@Ag/SAE coating was sprayed on the flexible PI film substrate, then the bending radius was kept at 3 mm (Figure S13), the bending−release cycle was performed 2000 times, and the change of its conductivity was recorded. As shown in conductivity Figure 7a, the conductivity of the Cu@Ag/SAE coating gradually decreased with increasing bending times. The conductivity of the F-40Cu@Ag/SAE film decreased to 71.4% after 2000 bending−release cycles. Similarly, the conductivity of the F-50Cu@Ag/SAE film decreased to 79.24%. F-60Cu@Ag/SAE and F-70Cu@Ag/SAE films maintained good stability as the filler was elevated. In particular, for the F-70Cu@Ag/SAE film, the conductivity retention was 98.91% at 500 cycles, 97.44% at 1000 cycles, and 95.42% at 1500 cycles. Ultimately, it decreased to 93.40% over 2000 cycles. The reason for this is that the silicone−acrylic emulsion has higher flexibility than Cu@Ag flakes, and after 2000 cycles of loading, the filler broke before the matrix (Figure 7b), increasing the resistance of the film, which in turn shows a decrease in conductivity. As the filler ratio increases, a perfect conductive pathway is formed in the film, and electrons can be transferred from other pathways despite the breakage of some of the Cu@Ag flakes. The F-70Cu@Ag/SAE films were used as resistive elements from Figure 7c and connected in a circuit with a small bulb and a 1.5 V battery. The comparison reveals that the brightness of the small bulb hardly changes after the initial state and 2000 bending−release cycles of the film. This indicated that the

https://doi.org/10.1021/acsomega.3c04404
ACS Omega 2023, 8, 37032−37042

conductive coating withstood 2000 bending−release cycles without fracture and maintained excellent conductivity. This can be verified in the cube resistance in Figure 7d, where the cube resistance only increased by 6.68% after 2000 bending−release cycles. The Cu@Ag/SAE film showed excellent flexibility in the experiment, indicating its great potential in the field of flexible wearables.

4. CONCLUSIONS

In summary, conductive fillers were prepared by wet ball milling and chemical plating methods. Cu@Ag/SAE films were successfully fabricated by using solution mixing and spraying techniques. The wet ball milling can rapidly refine the copper powder from granules to low-loose-density flakes, and facile electroless plating realizes Cu@Ag core−shell composites with only 13.7 wt % silver content to exhibit great oxidation resistance during aging under an air atmosphere, which improves the construction efficiency of electron transport paths in the films and imparts efficient conductivity and EMI SE and Joule heating performances. The conductivity and EMI SE of Cu@Ag/SAE films were tunable by varying the contents of conductive fillers. It is noteworthy that 50 wt % Cu@Ag flakes in a thin film were sufficient to reach the percolation threshold. In particular, the F-70Cu@Ag/SAE coating boasted a remarkable conductivity of 1073.61 S cm^{-1} and an ultrahigh EMI SE of 76.31 dB. Meanwhile, the film had a safe and efficient Joule heating performance with a saturation temperature of 112.1 °C at an applied voltage of 2 V. In addition, the film possessed excellent flexibility, maintaining a conductivity of 93.40% after a 3 mm bending radius and 2000 bending−release cycles. Therefore, the facile, environmentally friendly, scalable preparation method and outstanding comprehensive performance enabled the waterborne conductive composites to demonstrate great promise for the next generation of wearable and flexible electronics.

■ ASSOCIATED CONTENT

Supporting Information

The Supporting Information is available free of charge at https://pubs.acs.org/doi/10.1021/acsomega.3c04404.

SEM, FTIR, and XRD of the Cu flake; thickness measurements, Joule thermal property data, and bending−release digital photographs of Cu@Ag/SAE thin films; and EMI SE and Joule heating properties of Cu@Ag/SAE thin films in comparison with previous work (PDF)

■ AUTHOR INFORMATION

Corresponding Authors

Yong Zhang − *School of Materials Science and Engineering, Hefei University of Technology, Hefei 230009 Anhui, China; Key Laboratory of Advanced Functional Materials and Devices of Anhui Province, Hefei 230009, China; China International S&T Cooperation Base for Advanced Energy and Environmental Materials, Hefei 230009 Anhui,, China;* orcid.org/0000-0002-7625-2234; Email: zhangyong.mse@hfut.edu.cn

Yucheng Wu − *School of Materials Science and Engineering, Hefei University of Technology, Hefei 230009 Anhui, China; Key Laboratory of Advanced Functional Materials and Devices of Anhui Province, Hefei 230009, China; China International S&T Cooperation Base for Advanced Energy and Environmental Materials, Hefei 230009 Anhui,, China;* orcid.org/0000-0002-1549-0546; Email: ycwu@hfut.edu.cn

Authors

Zhongxin Huang − *School of Materials Science and Engineering, Hefei University of Technology, Hefei 230009 Anhui, China; Key Laboratory of Advanced Functional Materials and Devices of Anhui Province, Hefei 230009, China*

Huipeng Wang − *School of Materials Science and Engineering, Hefei University of Technology, Hefei 230009 Anhui, China; Key Laboratory of Advanced Functional Materials and Devices of Anhui Province, Hefei 230009, China*

Yuanyuan Li − *School of Materials Science and Engineering, Hefei University of Technology, Hefei 230009 Anhui, China; Key Laboratory of Advanced Functional Materials and Devices of Anhui Province, Hefei 230009, China*

Jiewu Cui − *School of Materials Science and Engineering, Hefei University of Technology, Hefei 230009 Anhui, China; Key Laboratory of Advanced Functional Materials and Devices of Anhui Province, Hefei 230009, China; China International S&T Cooperation Base for Advanced Energy and Environmental Materials, Hefei 230009 Anhui,, China;* orcid.org/0000-0003-4613-4795

Yan Wang − *School of Materials Science and Engineering, Hefei University of Technology, Hefei 230009 Anhui, China; Key Laboratory of Advanced Functional Materials and Devices of Anhui Province, Hefei 230009, China; China International S&T Cooperation Base for Advanced Energy and Environmental Materials, Hefei 230009 Anhui,, China;* orcid.org/0000-0003-1479-1715

Jiaqin Liu − *Key Laboratory of Advanced Functional Materials and Devices of Anhui Province, Hefei 230009, China; Institute of Industry & Equipment Technology, Engineering Research Center of Advanced Composite Materials Design & Application of Anhui Province, Hefei University of Technology, Hefei 230009, China; China International S&T Cooperation Base for Advanced Energy and Environmental Materials, Hefei 230009 Anhui,, China;* orcid.org/0000-0003-1663-7447

Complete contact information is available at: https://pubs.acs.org/10.1021/acsomega.3c04404

Notes

The authors declare no competing financial interest.

■ ACKNOWLEDGMENTS

This project is supported by the Science and Technology Major Project of Anhui Province (202003a05020007), the National Natural Science Foundation of China (Nos. 52072106 and U1810204), the Key R&D Projects of Anhui Province (202104b11020016), and the Natural Science Foundation of Anhui Province (2108085MB45). The authors would also like to thank the Higher Education Discipline Innovation Project "New Materials and Technology for Clean Energy" (B18018) for financial support. The authors would like to express their gratitude to Dr. Hui Huang from Beijing Xinchen Technology Co., Ltd. and Xirui Li from Anhui Jincen Composites Co., Ltd., for their valuable suggestions on the manuscript preparation.

REFERENCES

(1) Liu, Y.; Wu, Y.; Li, K.; Wang, J.; Zhang, C.; Ji, J.; Wang, W. Amorphous SnS nanosheets/graphene oxide hybrid with efficient dielectric loss to improve the high-frequency electromagnetic wave absorption properties. *Appl. Surf. Sci.* **2019**, *486*, 344−353.

(2) Wang, X.-Y.; Liao, S.-Y.; Wan, Y.-J.; Zhu, P.-L.; Hu, Y.-G.; Zhao, T.; Sun, R.; Wong, C.-P. Electromagnetic interference shielding materials: recent progress, structure design, and future perspective. *J. Mater. Chem. C* **2021**, *10* (1), 44−72.

(3) Zhang, Y.; Gu, J. A Perspective for Developing Polymer-Based Electromagnetic Interference Shielding Composites. *Nanomicro. Lett.* **2022**, *14* (1), No. 89, DOI: 10.1007/s40820-022-00843-3.

(4) Du, Y.; Wang, X.; Dai, X.; Lu, W.; Tang, Y.; Kong, J. Ultraflexible, highly efficient electromagnetic interference shielding, and self-healable triboelectric nanogenerator based on Ti3C2T MXene for self-powered wearable electronics. *J. Mater. Sci. Technol.* **2022**, *100*, 1−11.

(5) Guo, Y.; Li, K.; Hou, C.; Li, Y.; Zhang, Q.; Wang, H. Fluoroalkylsilane-Modified Textile-Based Personal Energy Management Device for Multifunctional Wearable Applications. *ACS Appl. Mater. Interfaces* **2016**, *8* (7), 4676−4683.

(6) Zheng, X.; Zhang, H.; Liu, Z.; Jiang, R.; Zhou, X. Functional composite electromagnetic shielding materials for aerospace, electronics and wearable fields. *Mater. Today Commun.* **2022**, *33*, No. 104498, DOI: 10.1016/j.mtcomm.2022.104498.

(7) Zhou, B.; Li, Z.; Li, Y.; Liu, X.; Ma, J.; Feng, Y.; Zhang, D.; He, C.; Liu, C.; Shen, C. Flexible hydrophobic 2D Ti3C2Tx-based transparent conductive film with multifunctional self-cleaning, electromagnetic interference shielding and joule heating capacities. *Compos. Sci. Technol.* **2021**, *201*, No. 108531, DOI: 10.1016/j.compscitech.2020.108531.

(8) Cheng, Y.; Seow, J. Z. Y.; Zhao, H.; Xu, Z. J.; Ji, G. A Flexible and Lightweight Biomass-Reinforced Microwave Absorber. *Nanomicro Lett.* **2020**, *12* (1), No. 125.

(9) Liu, Y.; Zhang, X.; Chen, X.; Wu, Y.; Zhang, C.; Wang, J.; Ji, J.; Li, K. Intense nonlinear dielectric and magnetic resonances of core−shell Ni@graphene composites and their improved microwave absorption properties. *J. Mater. Chem. C* **2021**, *9* (14), 4910−4920.

(10) Peng, T.; Wang, S.; Xu, Z.; Tang, T.; Zhao, Y. Multifunctional MXene/Aramid Nanofiber Composite Films for Efficient Electromagnetic Interference Shielding and Repeatable Early Fire Detection. *ACS Omega* **2022**, *7* (33), 29161−29170.

(11) Xu, J.; Chen, R.; Yun, Z.; Bai, Z.; Li, K.; Shi, S.; Hou, J.; Guo, X.; Zhang, X.; Chen, J. Lightweight Epoxy/Cotton Fiber-Based Nanocomposites with Carbon and Fe(3)O(4) for Electromagnetic Interference Shielding. *ACS Omega* **2022**, *7* (17), 15215−15222.

(12) Zhang, Y.; Ruan, K.; Gu, J. Flexible Sandwich-Structured Electromagnetic Interference Shielding Nanocomposite Films with Excellent Thermal Conductivities. *Small* **2021**, *17* (42), No. e2101951.

(13) Wan, Y. J.; Wang, X. Y.; Li, X. M.; Liao, S. Y.; Lin, Z. Q.; Hu, Y. G.; Zhao, T.; Zeng, X. L.; Li, C. H.; Yu, S. H.; et al. Ultrathin Densified Carbon Nanotube Film with "Metal-like" Conductivity, Superior Mechanical Strength, and Ultrahigh Electromagnetic Interference Shielding Effectiveness. *ACS Nano* **2020**, *14* (10), 14134−14145.

(14) Li, L.; Cao, Y.; Liu, X.; Wang, J.; Yang, Y.; Wang, W. Multifunctional MXene-Based Fireproof Electromagnetic Shielding Films with Exceptional Anisotropic Heat Dissipation Capability and Joule Heating Performance. *ACS Appl. Mater. Interfaces* **2020**, *12* (24), 27350−27360.

(15) Choi, H. K.; Lee, A.; Park, M.; Lee, D. S.; Bae, S.; Lee, S. K.; Lee, S. H.; Lee, T.; Kim, T. W. Hierarchical Porous Film with Layer-by-Layer Assembly of 2D Copper Nanosheets for Ultimate Electromagnetic Interference Shielding. *ACS Nano* **2021**, *15* (1), 829−839.

(16) Jia, Y.; Sun, R.; Pan, Y.; Wang, X.; Zhai, Z.; Min, Z.; Zheng, G.; Liu, C.; Shen, C.; Liu, X. Flexible and thin multifunctional waterborne polyurethane/Ag film for high-efficiency electromagnetic interference shielding, electro-thermal and strain sensing performances. *Compos. B. Eng.* **2021**, *210*, No. 108668.

(17) Fan, M.; Li, S.; Wu, L.; Li, L.; Qu, M.; Nie, J.; Zhang, R.; Tang, P.; Bin, Y. Natural rubber toughened carbon nanotube buckypaper and its multifunctionality in electromagnetic interference shielding, thermal conductivity, Joule heating and triboelectric nanogenerators. *Chem. Eng. J.* **2022**, *433*, No. 133499.

(18) Fan, M.; Xia, X.; Li, S.; Zhang, R.; Wu, L.; Qu, M.; Tang, P.; Bin, Y. Sustainable bacterial cellulose reinforced carbon nanotube buckypaper and its multifunctionality for electromagnetic interference shielding, Joule heating and humidity sensing. *Chem. Eng. J.* **2022**, *441*, No. 136103.

(19) Fu, C.; Sheng, Z.; Zhang, X. Laminated Structural Engineering Strategy toward Carbon Nanotube-Based Aerogel Films. *ACS Nano* **2022**, *16* (6), 9378−9388.

(20) Hu, P.; Lyu, J.; Fu, C.; Gong, W. B.; Liao, J.; Lu, W.; Chen, Y.; Zhang, X. Multifunctional Aramid Nanofiber/Carbon Nanotube Hybrid Aerogel Films. *ACS Nano* **2020**, *14* (1), 688−697.

(21) Chen, W.; Liu, L. X.; Zhang, H. B.; Yu, Z. Z. Kirigami-Inspired Highly Stretchable, Conductive, and Hierarchical Ti(3)C(2)T(x) MXene Films for Efficient Electromagnetic Interference Shielding and Pressure Sensing. *ACS Nano* **2021**, *15* (4), 7668−7681.

(22) Guo, Z.; Ren, P.; Wang, J.; Tang, J.; Zhang, F.; Zong, Z.; Chen, Z.; Jin, Y.; Ren, F. Multifunctional sandwich-structured magnetic-electric composite films with Joule heating capacities toward absorption-dominant electromagnetic interference shielding. *Compos. B. Eng.* **2022**, *236*, No. 109836.

(23) Wang, Q.-W.; Zhang, H.-B.; Liu, J.; Zhao, S.; Xie, X.; Liu, L.; Yang, R.; Koratkar, N.; Yu, Z.-Z. Multifunctional and Water-Resistant MXene-Decorated Polyester Textiles with Outstanding Electromagnetic Interference Shielding and Joule Heating Performances. *Adv. Funct. Mater.* **2019**, *29* (7), No. 1806819, DOI: 10.1002/adfm.201806819.

(24) Yang, S.; Yan, D.-X.; Li, Y.; Lei, J.; Li, Z.-M. Flexible Poly(vinylidene fluoride)-MXene/Silver Nanowire Electromagnetic Shielding Films with Joule Heating Performance. *Ind. Eng. Chem. Res.* **2021**, *60* (27), 9824−9832.

(25) Kim, C. K.; Lee, G.-J.; Lee, M. K.; Rhee, C. K. A novel method to prepare Cu@Ag core−shell nanoparticles for printed flexible electronics. *Powder Technol.* **2014**, *263*, 1−6.

(26) Tsai, C.-H.; Chen, S.-Y.; Song, J.-M.; Chen, I.-G.; Lee, H.-Y. Thermal stability of Cu@Ag core−shell nanoparticles. *Corros. Sci.* **2013**, *74*, 123−129.

(27) Liu, C.; Huang, X.; Zhou, J.; Chen, Z.; Liao, X.; Wang, X.; Shi, B. Lightweight and high-performance electromagnetic radiation shielding composites based on a surface coating of Cu@Ag nanoflakes on a leather matrix. *J. Mater. Chem. C* **2016**, *4* (5), 914−920.

(28) Jin, H.; Matsuhisa, N.; Lee, S.; Abbas, M.; Yokota, T.; Someya, T. Enhancing the Performance of Stretchable Conductors for E-Textiles by Controlled Ink Permeation. *Adv. Mater.* **2017**, *29* (21), No. 1605848, DOI: 10.1002/adma.201605848.

(29) Young Ryu, S.; Kwak, C.; Kim, J.; Kim, S.; Cho, H.; Lee, J. 3D-printable, lightweight, and electrically conductive metal inks based on evaporable emulsion templates jammed with natural rheology modifiers. *J. Colloid Interface Sci.* **2022**, *628* (Pt B), 758−767.

(30) Zeng, X.; He, P.; Hu, M.; Zhao, W.; Chen, H.; Liu, L.; Sun, J.; Yang, J. Copper inks for printed electronics: a review. *Nanoscale* **2022**, *14* (43), 16003−16032.

(31) Zhou, X.; Li, Y.; Fang, C.; Li, S.; Cheng, Y.; Lei, W.; Meng, X. Recent Advances in Synthesis of Waterborne Polyurethane and Their Application in Water-based Ink: A Review. *J. Mater. Sci. Technol.* **2015**, *31* (7), 708−722.

(32) Li, H.; Yuan, D.; Li, P.; He, C. High conductive and mechanical robust carbon nanotubes/waterborne polyurethane composite films for efficient electromagnetic interference shielding. *Composites, Part A* **2019**, *121*, 411−417.

(33) Jiao, C.; Sun, L.; Shao, Q.; Song, J.; Hu, Q.; Naik, N.; Guo, Z. Advances in Waterborne Acrylic Resins: Synthesis Principle,

https://doi.org/10.1021/acsomega.3c04404
ACS Omega 2023, 8, 37032−37042

Modification Strategies, and Their Applications. *ACS Omega* **2021**, *6* (4), 2443−2449.
(34) Qu, Y.-Y.; Zhang, S.-F. Preparation and characterization of novel waterborne antifouling coating. *J. Coat. Technol. Res.* **2012**, *9* (6), 667−674.
(35) Xu, Y.; Yang, Y.; Yan, D. X.; Duan, H.; Zhao, G.; Liu, Y. Gradient Structure Design of Flexible Waterborne Polyurethane Conductive Films for Ultraefficient Electromagnetic Shielding with Low Reflection Characteristic. *ACS Appl. Mater. Interfaces* **2018**, *10* (22), 19143−19152.
(36) Peng, M.; Qin, F. Clarification of basic concepts for electromagnetic interference shielding effectiveness. *J. Appl. Phys.* **2021**, *130* (22), No. 225108, DOI: 10.1063/5.0075019.
(37) Shuai, C.; He, C.; Peng, S.; Qi, F.; Wang, G.; Min, A.; Yang, W.; Wang, W. Mechanical Alloying of Immiscible Metallic Systems: Process, Microstructure, and Mechanism. *Adv. Eng. Mater.* **2021**, *23* (4), No. 2001098, DOI: 10.1002/adem.202001098.
(38) Suryanarayana, C. Mechanical Alloying: A Novel Technique to Synthesize Advanced Materials. *Research* **2019**, *2019*, No. 4219812.
(39) Moreno Baqueiro Sansao, B.; Kellar, J. J.; Cross, W. M.; Schottler, K.; Romkes, A. Comparison of surface energy and adhesion energy of surface-treated particles. *Powder Technol.* **2021**, *384*, 267−275.
(40) Jia, L.-C.; Sun, W.-J.; Zhou, C.-G.; Yan, D.-X.; Zhang, Q.-C.; Li, Z.-M. Integrated strength and toughness in graphene/calcium alginate films for highly efficient electromagnetic interference shielding. *J. Mater. Chem. C* **2018**, *6* (34), 9166−9174.
(41) Liu, P.; Hensen, E. J. Highly efficient and robust Au/MgCuCr2O4 catalyst for gas-phase oxidation of ethanol to acetaldehyde. *J. Am. Chem. Soc.* **2013**, *135* (38), 14032−14035.
(42) Liu, C.; Wu, W.; Wang, Y.; Wang, Z.; Chen, Q. Silver-coated thermoplastic polyurethane hybrid granules for dual-functional elastomer composites with exceptional thermal conductive and electromagnetic interference shielding performances. *Compos. Commun.* **2021**, *25*, No. 100719.
(43) Wang, J.; Li, Q.; Li, K.; Sun, X.; Wang, Y.; Zhuang, T.; Yan, J.; Wang, H. Ultra-High Electrical Conductivity in Filler-Free Polymeric Hydrogels Toward Thermoelectrics and Electromagnetic Interference Shielding. *Adv. Mater.* **2022**, *34* (12), No. e2109904.
(44) Song, Q.; Ye, F.; Yin, X.; Li, W.; Li, H.; Liu, Y.; Li, K.; Xie, K.; Li, X.; Fu, Q.; et al. Carbon Nanotube-Multilayered Graphene Edge Plane Core-Shell Hybrid Foams for Ultrahigh-Performance Electromagnetic-Interference Shielding. *Adv. Mater.* **2017**, *29* (31), No. 1701583, DOI: 10.1002/adma.201701583.

https://doi.org/10.1021/acsomega.3c04404
ACS Omega 2023, 8, 37032−37042